1

2   Detection of Ionospheric Alfvén Resonator Signatures in the Equatorial Ionosphere

3

4   Authors

5   Fernando Simões[1], Jeffrey Klenzing[1], Stoyan Ivanov[2], Robert Pfaff[1], Henry Freudenreich[1], Dieter

6   Bilitza[3,4], Douglas Rowland[1], Kenneth Bromund[1], Maria Carmen Liebrecht[1], Steven Martin[1], Peter

7   Schuck[1], Paulo Uribe[1], Tatsuhiro Yokoyama[1]

8

9   1 – NASA/GSFC, Heliophysics Science Division, Space Weather Laboratory (code 674), Greenbelt,
10 Maryland, USA

11 2 – Department of Physics, Georgia Institute of Technology, Atlanta, Georgia, USA

12 3 – NASA/GSFC, Heliophysics Science Division, Heliospheric Physics Laboratory (code 672),

13 Greenbelt, Maryland, USA

14 4 – George Mason University, Space Weather laboratory, Fairfax, Virginia, USA

15

16   **Abstract**

17   The ionosphere response resulting from minimum solar activity during cycle 23/24 was

18 unusual and offered unique opportunities for investigating space weather in the near-Earth

19 environment. We report ultra low frequency electric field signatures related to the ionospheric

20 Alfvén resonator detected by the Communications/Navigation Outage Forecasting System

21 (C/NOFS) satellite in the equatorial region. These signatures are used to constrain ionospheric

22 empirical models and offer a new approach for monitoring ionosphere dynamics and space

23 weather phenomena, namely aeronomy processes, Alfvén wave propagation, and troposphere-

24 ionosphere-magnetosphere coupling mechanisms.

25

1. Introduction

The period of low solar activity during the recent solar cycle 23/24 minimum was unique during the space age, offering exceptional conditions for investigating space weather in the near-Earth environment, namely ionospheric phenomena. This atypical long-lasting low solar activity is particularly suitable for investigating, from a different perspective, a variety of ionospheric and magnetospheric processes, namely waves in plasma. Here we report in situ ionospheric measurements taken in the equatorial region, namely Alfvén wave signatures related to known, yet unfamiliar, ionospheric resonance phenomena. These findings offer a new approach to assess ionospheric plasma density and dynamics, in particular above the F-peak, contributing to improve empirical models of the ionosphere.

Alfvén waves are low frequency oscillations that occur in an ionized fluid permeated by a magnetic field such as the Earth ionosphere or magnetosphere. Perturbations in plasma homogeneity produce ion motion, a restoring magnetic field tension takes place to balance particles inertia, and an oscillation is created, generating magnetohydrodynamic (MHD) waves. When the wave vector is parallel to the background magnetic field, Alfvén waves are transverse and termed shear Alfvén modes; when the wave vector is perpendicular to the background magnetic field, Alfvén waves are longitudinal and correspond to magnetosonic modes [e.g., *Lysak*, 1999]. To a first approximation, these waves are dispersionless. Local and global plasma density heterogeneities in the ionosphere and magnetosphere allow for formation of waveguide and resonator structures where magnetosonic and shear Alfvén waves propagate. For example, the ionospheric magnetosonic waveguide results from magnetosonic wave reflection about the ionospheric F-region, where the Alfvén index of refraction is the highest; magnetosonic waves can be guided thousands of kilometers in the ionosphere between the northern and southern

49 hemispheres due to ionospheric ducting [*Greifinger and Greifinger*, 1968]. MHD waves can also

50 be partially trapped in the vertical direction between the lower boundary of the ionosphere and

51 the magnetosphere, a resonance mechanism known as Ionospheric Alfvén Resonator (IAR)

52 [*Polyakov and Rapoport*, 1981]. So far, IAR signatures have been clearly observed on the

53 ground at mid and high latitudes [*Belyaev et al.*, 1990]; satellite-based observations in the auroral

54 region have been also claimed [*Grzesiak*, 2000; *Chaston et al.*, 2002]. We present in situ

55 ionospheric electric field measurements related to IAR distinctive signatures detected in the

56 equatorial region. These IAR electric field signatures offer complementary means for

57 ionospheric plasma density diagnostic, and also contribute for the investigation of ionosphere

58 dynamics and space weather monitoring. Besides, these findings corroborate independent

59 measurements claiming that ionospheric models have been significantly overestimating plasma

60 density under solar minimum conditions.

61

62 **2. Ionospheric Alfvén Resonator**

63 Specific ionospheric plasma density variations with altitude can form a resonant cavity

64 between the lower boundary of the ionosphere (~100 km) and an altitude of about one Earth

65 radius. MHD waves can be partially trapped and amplified in the vertical direction between the

66 two boundaries, producing distinctive resonance signatures in both Ultra and Extremely Low

67 Frequency (ULF-ELF) spectra, in the range 0.01-40 Hz. The IAR excitation source is likely

68 related to lightning or geomagnetic pulsations though irrefutable proof has yet to be established.

69 Particular spectral resonance structures have been considered evidence for IAR phenomena

70 [*Belyaev et al.*, 1990]. Subsequent measurements have expanded our knowledge of IAR

71 dynamics consistently [*Grzesiak*, 2000; *Chaston et al.*, 2002; *Bösinger et al.*, 2004; *Parent et al.*,

72   2010]. In addition to intrinsic spectral structures, the main characteristics of IAR shear Alfvén

73   waves include a vertical wave vector and horizontal oscillations of the electric and magnetic

74   fields. When losses are taken into account, coupling between the shear Alfvén and magnetosonic

75   modes is possible and the resonator response is more intricate (see complementary information

76   in the modeling section). Because a background magnetic field radial component, B_r, is required,

77   IAR excitation may only occur off the magnetic equator.

78   The Alfvén index of refraction, defined by

79    $$n_A = \frac{c}{V_A},$$ (1)

80

81   where c is the velocity of light in free space and V_A the Alfvén velocity in the medium, is

82   crucial to understand how the IAR functions. Shear Alfvén waves can be reflected in the

83   ionosphere, and consequently trapped, if sharp gradients (with respect to the wavelength) of the

84   refractive index occur. The Alfvén velocity is defined by

85

86    $$V_A = \frac{B}{\sqrt{\mu_o \rho}},$$ (2)

87

88   where B is the background magnetic field, ρ is the density of charged particles (e⁻, H^+, He^+,

89   and O^+), and μ_o is the permeability of vacuum. Since shear Alfvén modes propagate parallel to

90   the background magnetic field and the wave vector is approximately vertical inside the resonator,

91   the resonance effect is more pronounced at high latitudes, where the dip angle is larger and,

92   consequently, the magnetic field vertical component more important. Figure 1 shows typical

93   profiles of electron density, Alfvén velocity, and index of refraction, and also illustrates that the

94   resonator response occurs primarily close to the F-peak. The dashed line represents an

95   approximate profile often used for obtaining IAR analytical solutions; under such conditions, the

96   frequency and Q-factor of the resonator are [*Polyakov and Rapoport*, 1981; *Lysak*, 1999]

97

98   $$f_n = V_A \frac{n+1/4}{2(L+H)}$$ (3)

99   and

100   $$Q_n = \frac{1+L/H}{\pi\varepsilon},$$ (4)

101   where L and H are the length and scale height of the Alfvén velocity 'well', respectively,

102   $\varepsilon \equiv V_A^{min}/V_A^{max}$ is related to the depth of the well, and n=0,1,2,… is the eigenmode number.

103   Because the lower eigenmodes are often buried in the background noise, it is helpful calculating

104   the frequency difference between consecutive peaks, which is defined by

105

106   $$\Delta f \equiv \frac{V_A}{2(L+H)}.$$ (5)

107

108   The Q-factor of the resonator increases, i.e., better wave propagation conditions occur, when

109   the Alfvén velocity ionospheric well is deep, wide, and sharp. The threshold condition for wave

110   amplification in the IAR upper boundary, derived from resonator reflection and transmission

111   coefficients, is given by the inequality

112

113   $$\frac{\pi\varepsilon\omega H}{V_A} < 1,$$ (6)

114

115   where ω is the angular frequency of the propagating wave.

116   This condition is normally valid in the lower boundary of the resonator, and reflection

117   happens, because ∇n_A is sharp; shear Alfvén waves are nevertheless able to propagate down to

118   the ground not only because the ionospheric barrier is relatively thin and waves can emerge

119   below the D-region but also because good propagation conditions occur when Pedersen

120   conductivity matches the Alfvén wave impedance. Measurement of IAR parameters contributes

121   to ionosphere and magnetosphere characterization by solving the MHD inverse problem, i.e.,

122   inferring medium properties from wave dispersion data.

123

124   SUGGESTED LOCATION OF FIGURE 1

125

126   **3. C/NOFS Measurements**

127   The Communications/Navigation Outage Forecasting System (C/NOFS) satellite was

128   launched in April 2008 into a low inclination (13 degree) orbit of with perigee at 401 km and

129   apogee near 867 km [*de la Beaujardière et al.*, 2004], and has provided invaluable data to

130   investigate the ionospheric equatorial region electrodynamics, namely scintillations, plasma

131   depletions, neutral winds, aeronomy processes, and low frequency electromagnetic waves [*de la*

132   *Beaujardière et al.*, 2009; *Heelis et al.*, 2009; *Klenzing et al.*, 2011; *Simões et al.*, 2011a].

133   Among the scientific payload, the Vector Electric Field Instrument (VEFI) is used to investigate

134   electric and magnetic fields; VEFI consists of a three-axis double probe electric field detector

135   that provides continuous DC and AC electric field measurements, a magnetometer, and two

136   optical sensors for lightning detection [*Pfaff et al.*, 2010; *Holzworth et al.*, 2011]. The double

137   probe sensitivity in the ULF-ELF range is ~10 nVm^{-1}Hz$^{-1/2}$ for a sampling rate of 512 s^{-1}.

138   Spectrograms of the electric field meridional (vertical) and zonal (east-west) components

139   measured near the terminator during orbits 666-667 are shown in Figure 2. Sunset and satellite

140   eclipse occur at about 1507 and 1515 UT for orbit 666, and 1644 and 1652 UT for orbit 667. The

141   pattern resembling a fingerprint in the spectrograms is compatible with an IAR signature and is

142   visible in the bottom-left corner of each plot (1500-1512 and 1636-1648 UT), where the satellite

143   moves from 650 to 450 km altitude, approaching perigee. The peak amplitude is larger in the

144   zonal component because the IAR electric field is horizontal, consistent with model predictions.

145   The top right panel also shows lines extending deep in the night sector (1639-1705 UT). The

146   electric field spectral density is about 10 and 15 dB above the background noise in the

147   meridional and zonal components, respectively. The fuzzy, wide horizontal stripes visible close

148   to 8, 14, 20, 26, and 32 Hz in the plots are Schumann resonance modes, ELF signatures of the

149   longitudinal mode of the earth-ionosphere cavity [*Simões et al.*, 2011a].

150

151   SUGGESTED LOCATION OF FIGURE 2

152

153   Figure 3 illustrates a magnification of Figure 2 to emphasize a narrow spectral line detected

154   during orbit 667 and flagged by arrows. A few spectra in the vicinity of the event are showing

155   the background signal. The event starts at about 16:41:24 UT and lasts ~0.5 s. In addition to the

156   distinctive waveform bearing evidence for dispersion and amplitude modulation, the spectral line

157   presents a few more noteworthy characteristics: (i) a dozen peaks overlapping the fingerprint

158   signature, i.e., peak frequencies of the event match the fingerprint spectral features; (ii) the Q-

159   factor is roughly twice that of the fingerprint; (iii) a peak amplitude of ~0.5 $\mu Vm^{-1}Hz^{-1/2}$ that

160   seems almost constant in the frequency range 1-15 Hz and is about 2.5 times larger than in the

161 fingerprint; (iv) the peak is absent above 14 Hz and only reappears beyond 20 Hz modulated by

162 Schumann resonance modes; (v) like in the fingerprint, the ratio of the electric field zonal to

163 meridional component is ~2. Finally, peak distribution shows Δf~1.1 Hz and f_{th}~14 Hz, where f_{th}

164 is a threshold frequency. A closer inspection also shows a morphological transition occurring

165 around 14 Hz in the spectrograms, where the resonance grows fainter.

166   Figure 4 presents the electric field intensity, E, and Δf variation when the resonator signature

167 is observed in orbit 667, i.e., about the terminator, in the range 0-20 Hz. Both E and Δf clearly

168 increase within the time span considered. The solid lines represent modeling results discussed in

169 section 4. Figure 5 shows an even stronger IAR signature with larger frequency detected during

170 orbit 694. Another interesting feature seen both in Figures 2 and 5 is the markedly asymptotic

171 increase of frequency when the satellite is moving toward ellipse.

172

173   SUGGESTED LOCATION OF FIGURES 3 AND 4

174

175   The IAR signature seen near dusk is also detected at dawn when orbit conditions are

176 reversed, i.e., perigee occurs in the early morning sector, as shown in Figure 6. In addition to

177 IAR frequency decrease near sunrise, the plot shows narrow lines imprinted in the structured hiss

178 visible in the meridional component during nighttime. It is worth mentioning that Δf in the

179 structured hiss is only slightly larger than near dawn, and up to 20 lines are apparent. These

180 observations were made during orbit 2898, in 28-29 October 2008.

181

182   SUGGESTED LOCATION OF FIGURE 5

183

4. Modeling

Although the IAR analytical theory is valuable for providing perceptive, approximate solutions, numerical modeling is required when real ionospheric profiles are chosen (cf. Figure 1). An algorithm based in the finite element method has been recurrently used to solve low frequency electromagnetic wave propagation phenomena (transient, eigenmode, harmonic, and parametric analyses) in the surface-ionosphere cavity of the Earth and other planets [*Simões et al.*, 2007, 2008a, 2008b, 2009]; the algorithm has been upgraded with the fluid dynamics formalism for solving MHD equations and computing IAR eigenfunctions. The IAR numerical model is based on the linearized, cold, multi-fluid description for electrons and ions in collisional plasma [*Lysak*, 1999]. The algorithm separates the longitudinal and transverse components with respect to the geomagnetic field, utilizes altitude as the independent variable, and computes the shear Alfvén and magnetosonic eigenmodes. This model employs four parameterizations of the medium that are dependent of the Pedersen (σ_P) and Hall (σ_H) conductivities, and of the transverse heterogeneity current ($j_\perp$): (M1) lossless medium ($\sigma_P=\sigma_H=j_\perp=0$); (M2) lossy medium without mode coupling ($\sigma_P\neq0$, $\sigma_H=j_\perp=0$); (M3) lossy medium with coupling ($\sigma_P\neq0$, $\sigma_H\neq0$, $j_\perp=0$); (M4) lossy medium with coupling and local transverse heterogeneity ($\sigma_P\neq0$, $\sigma_H\neq0$, $j_\perp\neq0$). Hall conductivity introduces a driving action in the resonator through coupling between the shear Alfvén and magnetosonic modes. Magnetic diffusivity due to parallel conductivity and transverse heterogeneity often generates instabilities in the resonator [*Lysak and Song*, 2002]. Medium parameterization requires information about the background magnetic field, collision frequency, ion composition, and electron density to derive the Alfvén velocity and conductivity tensor. The amplitude and vertical component of the magnetic field are evaluated from the International Geomagnetic Reference Field (IGRF-11) model [*Finlay et al.*, 2010]. The electron

207 density and ion composition are computed from the International Reference Ionosphere (IRI-

208 2007) model [*Bilitza and Reinisch*, 2009]. We also run the numerical model with the most recent

209 release (IRI-2011) to contrast IRI performance improvements. The effective collision frequency

210 is derived either from the International Standard Atmosphere (ISA) or from the Naval Research

211 Laboratory Mass Spectrometer Incoherent Scatter radar (NRLMSIS-E-00) empirical model,

212 which provides composition, temperature, and density distribution of neutrals [*Lide et al.*, 2010;

213 *Picone et al.*, 2002]. To a first approximation, medium parameterization inaccuracy is due to

214 electron density and ion composition uncertainty rather than to that of magnetic field or collision

215 frequency [*Simões et al.*, 2009]. The eigenfrequencies computed with the numerical model

216 (configuration M3) are shown in Figure 4 along with C/NOFS results. Model parameters are

217 evaluated against electron density and ion composition profiles considering various constraints

218 from IRI and the Ion Velocity Meter (IVM) data recorded onboard C/NOFS: (P0) IRI-2007

219 default parameterization; (P1) IRI density profile normalized against IVM plasma density

220 recorded during fingerprint observation (altitude ~500 km); (P2) IRI density and ion composition

221 profiles normalized against IVM data under conditions defined in P1; (P3) composite electron

222 density profile combining IVM mean density in the altitude range between 400 and 850 km (a

223 full discussion of the monthly and seasonal averages can be found in *Klenzing et al.* [2011]) and

224 IRI elsewhere; (P4) composite electron density and ion composition profiles under conditions

225 defined in P3; (P5) profile similar to P4 but with the IVM density distribution decreased by one

226 standard deviation; (P6) IRI-2011 default parameterization. Because the density profiles cannot

227 be fully reconstructed from 2008 due to uneven data coverage, the June solstice 2009 values are

228 used for the purpose of this study; this is nevertheless appropriate since measurements during

229 2008 and 2009 are closer to each other than they are to the IRI predictions for either year.

5. Discussion

The existence of an ionospheric resonator that is able to trap shear Alfvén waves was predicted theoretically and later identified in spectral resonance structures in the ULF range [*Polyakov and Rapoport*, 1981; *Belyaev et al.*, 1990]. Since then, IAR multiple spectral lines have been reported both on the ground [*Bösinger et al.*, 2004; *Parent et al.*, 2010], at mid and high latitudes, and onboard satellites in the auroral region [*Grzesiak*, 2000; *Chaston et al.*, 2002]. C/NOFS data extends IAR signature detection to the low-latitude regions, where the shear Alfvén mode is much less effective. VEFI is nevertheless able to detect IAR signatures because plasma density is smaller during low solar activity and C/NOFS coverage extends to mid magnetic latitudes as well.

According to modeling, high Δf and Q-factor offer better conditions for IAR fingerprint identification because peaks are stronger and better resolved. Ideally, the most favorable conditions to observe the IAR spectral structures onboard C/NOFS occur close to the F-peak, off the magnetic equator, during nighttime, and low solar activity because $\Delta f \propto B_r / \sqrt{\rho}$. Close to the terminator, because the background noise remains limited and strong refraction happens, dusk and dawn offer privileged conditions for observing the IAR signature (Figures 2 and 6). The frequency increasing near the terminator in orbits 666, 667, and 694 is most likely due to a fast, strong variation of plasma density in the ionosphere. A similar, reversed effect is seen in orbit 2898 near dawn. Supplementary material combining audio and video formats of the ELF spectrograms can be found here (LINK TO REPOSITORY SERVER). In addition to familiar, typical ionospheric transient phenomena such as whistlers, tweeks, chorus, and hiss, the low frequency sound with pitch increasing - a sort of reversed whistler effect - is a distinctive characteristic of the IAR signature related to plasma density strong decreasing near the

253 terminator. The sound related to the IAR signature shows better quality when the signal is

254 processed with a low pass filter. Although consistent with source power increasing, the electric

255 field enhancement seen in Figure 4 is likely due to improvements of resonator efficiency, i.e.,

256 sharper boundaries. The IAR signature is detected preferentially at low altitude, e.g., below 600

257 km, when the satellite is clearly inside the resonator and where better propagation conditions

258 happen.

259   Ground measurements of ULF electric and magnetic fields are usually suitable for deriving

260 not only IAR frequencies but also the Q-factor, from which resonator efficiency is inferred.

261 Computation of IAR spectral peak full width at half maximum provides a reasonable estimate of

262 cavity losses; a Q-factor in the order of 10 has been reported on the ground [*Belyaev et al.*,

263 1990]. Following a similar approach, we obtain Q-factors in the range 15-20 for most orbits and

264 ~30 for the narrow event reported in orbit 667. Qualitatively, these results seem plausible and

265 consistent with equation (4). However, the Q-factor computed with the numerical model (either

266 M2 or M3) overestimates observations considerably ($Q \equiv Re(f)/2Im(f) \sim 50$). Additionally,

267 neither plasma density and composition variability nor uncertainty in collision frequency is able

268 to bringing measurements and modeling to a reasonable agreement. Configuration M4 does not

269 seem to provide a reasonable agreement either despite some uncertainty in the $j_\perp$ parameter. To

270 assess the collision frequency uncertainty we use both ISA and NRLMSIS-E-00 models of the

271 neutrals but difference between the computed Q-factors is small. However, anomalously low

272 solar extreme-ultraviolet irradiance and thermospheric density during solar activity minimum

273 23/24 have been reported [*Solomon et al.*, 2010; *Emmert et al.*, 2010], suggesting that such a

274 contracted atmosphere may have modified the shape of the collision frequency profile

275 significantly.

276   As on the ground, the lowest Schumann resonance peaks are stronger than spectral resonance

277   structures attributed to IAR phenomena. During the day, IAR signatures are not easily detected

278   from orbit; under such conditions, the resonator is ineffective or, less likely, shows dense lines

279   that cannot be resolved by VEFI and then regarded as noise. During nighttime, IAR lines are

280   frequently visible (E~0.2 $\mu Vm^{-1}Hz^{-1/2}$) unless masked by the wider, stronger Schumann

281   resonance modes (E~0.5 $\mu Vm^{-1}Hz^{-1/2}$); on the ground, for comparison purposes, magnetic field

282   amplitude of IAR (at high latitude) and Schumann resonance are typically 0.1 and 1 pT,

283   respectively.

284   According to IAR theory, the electric field of the shear Alfvén mode should be horizontal.

285   Figures 2 and 5 show that the electric field horizontal (zonal) component is indeed dominant but

286   a vertical component is also present. A comprehensive assessment is impracticable because the

287   electric field component along the geomagnetic field and magnetic field data are not available at

288   that time. Nevertheless, vertical and horizontal components are clearly observed, suggesting a

289   coupling between shear Alfvén and magnetosonic modes.

290   Several natural mechanisms have been proposed regarding IAR excitation, including

291   lightning [*Surkov et al.*, 2006; *Shalimov and Bösinger*, 2008], transient luminous events, e.g,

292   sprites [*Sukhorukov and Stubbe*, 1997], and ionospheric-magnetospheric plasma waves, e.g.,

293   geomagnetic pulsations [*Lekhtinen et al.*, 1995; *Lysak and Song*, 2003]. The IAR artificial

294   excitation has also been claimed by means of ULF-ELF transmitters that match the resonator

295   frequency or by changing the macroscopic parameters of the ionosphere with radar pulses

296   [*Trakhtengertz et al.*, 2000]. However, the cause-effect relation between excitation source and

297   wave emission is difficult to establish and the subject remains unsolved. For example,

298   geomagnetic pulsations (e.g., Pc1, Pc2, and Pi1) may play multiple roles in generation, filtration,

299 modulation, or propagation phenomena in IAR dynamics [*Demekhov et al.*, 2000; *Prikner et al.*,

300 2004]. It is unlikely these mechanisms play similar roles at high and low latitudes because

301 particle precipitation is more important in the auroral region and lightning is concentrated close

302 to the equator. Although the narrow event observed during orbit 667 (Figure 3) bears

303 resemblance to Pc1 waves, namely range of frequency and amplitude modulation, we could not

304 establish a direct connection to lightning, particle precipitation, or geomagnetic activity.

305 Nevertheless, the sudden peak amplitude transition at $f_{th}\sim14$ Hz seems meaningful and is perhaps

306 related to medium transparency conditions in the top-side of the ionosphere defined in equation

307 (6). The significant increase of both the Q-factor and the electric field during the event (Figure 4)

308 is consistent with a narrow band electromagnetic source because the background noise remains

309 unaltered, suggesting that feedback amplification occurs [*Pokhotelov et al.*, 2001*; Lysak and*

310 *Song*, 2002]. The threshold condition for wave amplification defined in equation (6) can be used

311 for computing the cutoff frequency and constraining density profile parameterization.

312 Another interesting structure is seen during nighttime in the vertical/meridional component

313 during orbit 2898 (Figure 6). The presence of multiple narrow lines imprinted in hiss is

314 intriguing because Δf is commensurate with the IAR signature and almost 20 peaks are seen, but

315 the structure is noticeable in the vertical rather than horizontal component. Although in depth

316 assessments are necessary, we hypothesize this structure corresponds to the magnetosonic mode

317 since Δf is similar to that of IAR and an electric field vertical component prevails. The

318 observation of these resonance lines seems to require generation of strong hiss, possibly

319 associated to plasma turbulence or better propagation conditions in the medium (e.g., ionospheric

320 ducting). This feature could alternatively be related to processes occurring elsewhere and

321 enhanced by an increasing of local ionospheric turbulence. Additionally, the lower cutoff at ~25

322 Hz is close to the O^+ gyrofrequency and its shape somewhat resembles to that of the ion density,

323 suggesting lower hybrid modes may play a role. Either way, investigation of hiss structure

324 characteristics may lead to a better understanding of possible magnetosonic and shear Alfvén

325 mode coupling but is not the main purpose of this work.

326

327 SUGGESTED LOCATION OF FIGURE 6

328

329   Figure 7 shows a comparison between IAR model predictions considering IRI-2007 default

330 parameterization and VEFI measurements made in 31 May 2008, corresponding to about 15

331 orbits. The signature is visible and better resolved in VEFI data when Δf is larger. Alternation

332 between high and low peaks is related to magnetic field asymmetry with respect to the

333 geographic equator and minima refer to magnetic equator crossings. The IAR frequency

334 measured by VEFI is at least 5 times larger than model predictions (cf. Figure 4), suggesting that

335 IRI is significantly overestimating plasma density under solar minimum conditions, in line with

336 independent assessments [*Heelis et al.*, 2009; *Lühr and Xiong*, 2010; *Vlasov and Kelley*, 2010];

337 IRI predictions of density and composition are worst close to the terminator, too [*Klenzing et al.*,

338 2011]. Additionally, the increase in Δf is also steeper than IRI predictions, suggesting larger

339 density gradients near the terminator, a conclusion also drawn for the D-region from

340 observations onboard balloons for different solar activity [*Simões et al.*, 2009, 2011c]. Although

341 the modifications introduced in IRI profiles - taking into account plasma density and

342 composition as measured by C/NOFS - provide larger Δf, additional corrections are necessary to

343 IRI for fitting IAR results. Profiles P1-P5 show a better − though insufficient − agreement

344 between IAR features and the ionospheric plasma environment than that of uncorrected IRI

345   parameterization (P0). According to P1-P5, all corrections increase Δf but the resonator seems

346   more sensitive to composition and top-side profile shape than plasma density uncertainty,

347   because H^+ fraction is significantly underestimated and the density profile is sharper than IRI

348   predictions above 500 km. These results show that Δf is more sensitive to profile shape than

349   plasma density or composition, a result also corroborated by the analytical approximation

350   ($\Delta f \propto (L + H)^{-1}$ and $\Delta f \propto \rho^{-1/2}$). Since ground measurements are more frequent and reliable

351   than above the F-peak, it is not surprising that IRI is less accurate for the topside ionosphere.

352   Additionally, unlike radar networks and ground-based ionosonde data that usually imply constant

353   latitude and longitude, topside ionosonde [e.g., *Benson and Bilitza*, 2009] and in situ

354   measurements [e.g., *Klenzing et al.*, 2011] are trajectory dependent. Most likely, corrections to

355   plasma density during the 23/24 solar minimum are also necessary below the F-peak, as

356   suggested by IVM measurements above 400 km [*Klenzing et al.*, 2011]. Although insufficient,

357   IRI-2011 shows an improvement compared to older models (P6 vs. P0). Since modification of

358   the electron density profile by one standard deviation (P4 vs. P5) brings modeling and

359   measurements to a much better agreement, a statistical study of IAR features detected throughout

360   the mission is necessary because IRI usually provides monthly averages.

361

362   SUGGESTED LOCATION OF FIGURE 7

363

364   Modeling also suggests that equatorial ionospheric spread-F should have significant impact

365   in IAR structures due to sharp, large transition in plasma density. Although no clear evidence of

366   IAR sudden frequency variation due to spread-F phenomena has been found in C/NOFS data so

367   far, the numerical model predicts Δf increasing by as much as a factor of 5 when plasma density

368 decreases by 2 orders of magnitude, depending on the size of the bubble. The Q-factor also

369 increases significantly. Therefore, IAR fingerprint characterization would be also useful for

370 inferring spread-F vertical extension.

371   The characterization of IAR signatures contributes to the investigation of ionosphere

372 dynamics. In some cases, the following parameters can be derived from ELF measurements: Δf,

373 Q, and f_{th}. In general, the analytical profile includes four variables: ε, L, H, and V_A, where the

374 Alfvén velocity is a function of plasma density and composition. The system is underdetermined

375 and additional constraints are necessary, e.g., the plasma density and composition. Moreover, the

376 analytical profile is unrealistic and intricate plasma distributions must be considered. Although

377 challenging, the most practical way of inferring the density profiles is by solving the MHD

378 inverse problem considering fingerprint signatures as modeling constraints – in practice, the

379 more reasonable approach is solving the direct MHD problem iteratively to determine the best fit

380 for IAR data [Simões et al., 2011b]. In such a case, Δf_n and Q_n variation with the eigenmodes

381 should be used instead of mean values. For example, the Q-factors measured in orbit 667 show a

382 small, steady increasing with the eigenmodes, and Δf degeneracy is removed when plasma

383 density above the F-peak deviates from an exponential profile or medium losses are taken into

384 account. Since plasma density irregularities also produce uneven Δf distributions, IAR detailed

385 characterization eventually provides multiple Δf_n, Q_n constraints for MHD inverse problem

386 solutions, which are useful for determining the plasma composition and density profile, as well

387 as the total electron content. Future studies combining both ULF and high frequency techniques

388 such as GPS, radar, and radio occultation might provide even better approaches to constrain

389 plasma density and composition distributions, in particular close to the terminator.

390

6. Conclusion

Ionospheric in situ measurements onboard C/NOFS satellite show, for the first time, IAR signatures in the equatorial region. We derive frequency peak distribution and Q-factors of the resonator from IAR representative signatures, which contribute to a better characterization of ionospheric plasma dynamics at low latitude. Measurements onboard C/NOFS also show a peculiar, narrow event and structured hiss consisting of multiple lines possibly related to IAR dynamics, but their full significance, possibly related to modes coupling and feedback amplification mechanisms, requires further investigation. The IAR signature identified in ELF spectrograms can be used for inferring both medium properties and dynamics of the ionosphere. A MHD numerical model combining various parameterizations suggests that IAR is a resourceful tool for deriving plasma density profiles and investigating ionospheric irregularities; the model also confirms that during low solar activity IRI is not only overestimating plasma density but responding slowly to density gradients near the terminator, in line with independent assessments. Identification of IAR signatures at low latitude by C/NOFS is unexpected and valuable, offering new means for investigating the top-side equatorial ionosphere, namely plasma dynamics and interaction with the magnetosphere and solar wind. IAR signatures can be used to constrain not only plasma total density and composition of the ionosphere but also the shape of the profile, taking advantage of the valuable C/NOFS electric field dataset. Future developments should include a statistical analysis throughout the mission to identify geographical, seasonal, and solar wind/magnetospheric related characteristics.

7. Acknowledgements

8. References

Belyaev, P.P., S.V. Polyakov, V.O. Rapoport, and V.Yu. Trakhtengerts (1990), The ionospheric Alfvén resonator, *J. Atmos. Terr. Phys.*, 52, 781-788.

Benson, R.F., and D. Bilitza (2009), New satellite mission with old data: Rescuing a unique data set, *Radio Sci.*, 44, RS0A04, doi: 10.1029/2008RS004036.

Bilitza, D., and B.W. Reinisch (2009), International Reference Ionosphere 2007: Improvements and new parameters, *Adv. Space. Res.*, 44, 701-706.

Bösinger, T., A.G. Demekhov, and V.Y. Trakhtengerts (2004), Fine structure in ionospheric Alfvén resonator spectra observed at low latitude (L=1.3), *Geophys. Res. Lett.*, 31, L18802, doi:10.1029/2004GL020777.

437

438 Chaston, C.C., et al. (2002), Electron acceleration in the ionospheric Alfven resonator, *J.*

439 *Geophys. Res.*, 107, 1413, doi:10.1029/2002JA009272.

440

441 de la Beaujardière, O. et al. (2004), C/NOFS: a mission to forecast scintillations, *J. Atmos. Sol.*

442 *Terr. Phys.*, 66, 1573-1591.

443

444 Demekhov, A.G., V.Yu. Trakhtengerts, and T. Bösinger (2000), Pc 1 waves and ionospheric

445 Alfvén resonator: generation or filtration?, *Geophys. Res. Lett.*, 27, 3805-3808.

446

447 Emmert, J.T., J.L. Lean, and J.M. Picone (2010), Record-low thermospheric density during the

448 2008 solar minimum, *Geophys. Res. Lett.*, 37, L12102, doi: 10.1029/2010GL043671.

449

450 Finlay, C.C., et al. (2010), International Geomagnetic Reference Field: the eleventh generation,

451 *Geophys. J. Int.*, 183, 1216-1230.

452

453 Greifinger, C., and P.S. Greifinger (1968), Theory of hydromagnetic propagation in ionospheric

454 waveguide, *J. Geophys. Res.*, 73, 7473-7490, doi: 10.1029/JA073i023p07473.

455

456 Grzesiak, M. (2000), Ionospheric Alfvén resonator as seen by Freja satellite, *Geophy. Res. Lett.*,

457 27, 923-926.

458

459   Heelis, R.A., W.R. Coley, A.G. Burrell, M.R. Hairston, G.D. Earle, M.D. Perdue, R.A.

460   Power, L.L. Harmon, B.J. Holt, and C.R. Lippincott (2009), Behavior of the O+/H+ transition

461   height during the extreme solar minimum of 2008, *Geophys. Res. Lett.*, 36, L00C03, doi:

462   10.1029/2009GL038652.

463

464   Holzworth, R.H., M.P. McCarthy, R.F. Pfaff, A.R. Jacobson, W.L. Willcockson, and D.E.

465   Rowland (2011), Lightning-generated whistler waves observed by probes on the

466   Communication/Navigation Outage Forecast System satellite at low latitudes, *J. Geophys. Res.*,

467   116, A06306, doi: 10.1029/2010JA016198.

468

469   Klenzing, K., F. Simões, S. Ivanov, R.A. Heelis, D. Bilitza, R. Pfaff, and D. Rowland (2011),

470   Topside equatorial ionospheric density and composition during and after extreme solar

471   minimum, *J. Geophys. Res.*, 116, A12330, doi:10.1029/2011JA017213.

472

473   Lekhtinen, N.G., G.A. Markov, and S.M. Fainstein (1995), Excitation of an ionospheric Alfvén

474   resonator by a plasma wave discharge, *Radiophys. Quantum El.*, 38, 204-207.

475

476   Lide, D.R. et al. (2010), CRC Handbook of Chemistry and Physics, 90th edition, Taylor and

477   Francis, Boca Raton, Florida.

478

479   Lühr, H., and C. Xiong (2010), IRI-2007 model overestimates electron density during the 23/24

480   solar minimum, *Geophys. Res. Lett.*, 37, L23010, doi: 10.1029/2010GL045430.

481

482   Lysak, R., Propagation of Alfvén waves through the ionosphere: Dependence on ionospheric

483   parameters, *J. Geophys. Res.*, 104, 10017-10030, doi: 10.1029/1999JA900024 (1999).

484

485   Lysak, R.L., and Y. Song (2002), Energetics of the ionospheric feedback interaction, *J. Geophys.*

486   *Res.*, 107, doi: 10.1029/2001JA000308.

487

488   Lysak, R. L., and Y. Song (2003), Kinetic theory of the Alfvén wave acceleration of auroral

489   electrons, *J. Geophys. Res.*, 108, A48005, doi: 10.1029/2002JA009406.

490

491   Parent, A., I.R. Mann, and I.J. Rae (2010), Effects of substorm dynamics on magnetic signatures

492   of the ionospheric Alfvén resonator, *J. Geophys. Res.*, 115, A02312,

493   doi:10.1029/2009JA014673.

494

495   Picone, J.M., A.E. Hedin, D.P. Drob, and A.C. Aikin (2002), NRLMSISE-00 empirical model of

496   the atmosphere: Statistical comparisons and scientific issues, *J. Geophys. Res.*, 107, A121468,

497   doi: 10.1029/2002JA009430.

498

499   Pokhotelov, O.A., V. Khruschev, M. Parrot, S. Senchenkov, and V.P. Pavlenko (2001),

500   Ionospheric Alfvén resonator revisited: Feedback instability, *J. Geophys. Res.*, 106, 25813-

501   25824.

502

503   Polyakov, S.V., and V.O. Rapoport (1981), Ionospheric Alfvén resonator, *Geomagn. Aeron.*, 21,

504   610-614.

505

506 Pfaff, R., et al. (2010), Observations of DC electric fields in the low-latitude ionosphere and their

507 variations with local time, longitude, and plasma density during extreme solar minimum, *J.*

508 *Geophys. Res.*, 115, A12324, doi:10.1029/2010JA016023.

509

510 Prikner, K., K. Mursula, J. Kangas, R. Kerttula, and F.Z. Feygin (2004), An effect of the

511 ionospheric Alfvén resonator on multiband Pc1 pulsations, *Ann. Geophys.*, 22, 643–651.

512

513 Shalimov, S., and T. Bösinger (2008), On distant excitation of the ionospheric Alfvén resonator

514 by positive cloud-to-ground lightning discharges, *J. Geophys. Res.*, 113, A02303,

515 doi:10.1029/2007JA012614.

516

517 Simões, F., et al. (2007), A new numerical model for the simulation of ELF wave propagation

518 and the computation of eigenmodes in the atmosphere of Titan: did Huygens observe any

519 Schumann resonance?, *Planet. Space Sci.*, 55, 1978-1989.

520

521 Simões, F., et al. (2008a), The Schumann resonance: a tool for exploring the atmospheric

522 environment and the subsurface of the planets and their satellites, *Icarus*, 194, 30-41.

523

524 Simões, F., et al. (2008b), Electromagnetic wave propagation in the surface-ionosphere cavity of

525 Venus, *J. Geophys. Res.*, 113, E07007, doi: 10.1029/2007JE003045.

526

527 Simões, F., J.-J. Berthelier, M. Godefroy, and S. Yahi, (2009), Observation and modeling of the

528 Earth-ionosphere cavity electromagnetic transverse resonance and variation of the D-region

529 electron density near sunset, *Geophys. Res. Lett.*, 36, L14816, doi: 10.1029/2009GL039286.

530

531 Simões, F., J.-J. Berthelier, R. Pfaff, D. Bilitza, and J. Klenzing (2011c), Monitoring D-region

532 variability from lightning measurements, General Assembly and Scientific Symposium, 2011

533 XXXth URSI, pp.1-4, 13-20 Aug. 2011, doi: 10.1109/URSIGASS.2011.6050887.

534

535 Simões, F., R. F., Pfaff, J.-J., Berthelier, and J. Klenzing, (2011b), A review of low frequency

536 electromagnetic wave phenomena related to tropospheric-ionospheric coupling mechanisms,

537 *Space Sci. Rev.*, doi: 10.1007/s11214-011-9854-0 (in press)

538

539 Simões, F., R. F. Pfaff, and H. Freudenreich (2011a), Observation of Schumann resonances in

540 the Earth's ionosphere, *Geophys. Res. Lett.,* 38, L22101, doi:10.1029/2011GL049668.

541

542 Solomon, S.C., T.N. Woods, L.V. Didkovsky, J.T. Emmert, and L. Qian (2010), Anomalously

543 low solar extreme-ultraviolet irradiance and thermospheric density during solar minimum,

544 *Geophys. Res. Lett.*, 37, L16103, doi: 10.1029/2010GL044468.

545

546 Sukhorukov, A.I., and P. Stubbe (1997), Excitation of the lightning Alfven resonator by strong

547 lightning discharges, *Geophys. Res. Lett.*, 24, 829-832.

548

549   Surkov, V.V., M. Hayakawa, A.Y. Schekotov, E.N. Fedorov, and O.A. Molchanov (2006),

550   Ionospheric Alfvén resonator excitation due to nearby thunderstorms, *J. Geophys. Res.*, 111,

551   A01303, doi:10.1029/2005JA011320.

552

553   Trakhtengertz, V.Y., P.P. Belyaev, S.V. Polyakov, A.G. Demekhov, and T. Bosinger (2000),

554   Excitation of Alfvén waves and vortices in the ionospheric Alfvén resonator by modulated

555   powerful radio waves, *J. Atmos. Sol. Terr. Phys.*, 62, 231-238.

556

557   Vlasov, M.N., and M.C. Kelley (2010), Crucial discrepancy in the balance between extreme

558   ultraviolet solar radiation and ion densities given by the international reference ionosphere

559   model, *J. Geophys. Res.*, 115, A08317, doi: 10.1029/2009JA015103.

560

563   Figures
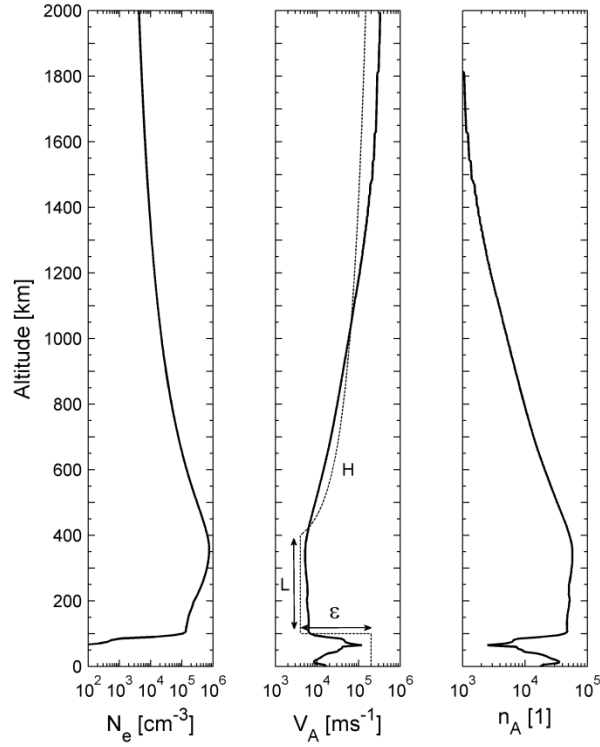
564

565   Figure 1: Low latitude typical ionospheric profiles of (from left to right) electron density (N_e),

566   Alfvén velocity (V_A), and index of refraction (n_A). The dashed line represents an Alfvén velocity

567   theoretical profile often used for obtaining IAR analytical solutions, where L, H, and ε refer to

568   the length, scale height, and depth of the Alfvén velocity 'well' ($V_A^2(z) = V_A^{2\,min}/(\varepsilon^2 + e^{-z/H})$

569   above z~400 km). Commonly, most IAR power is confined in the altitude range 100-500 km and

570   ε~0.01, L~300 km, and H~300 km.
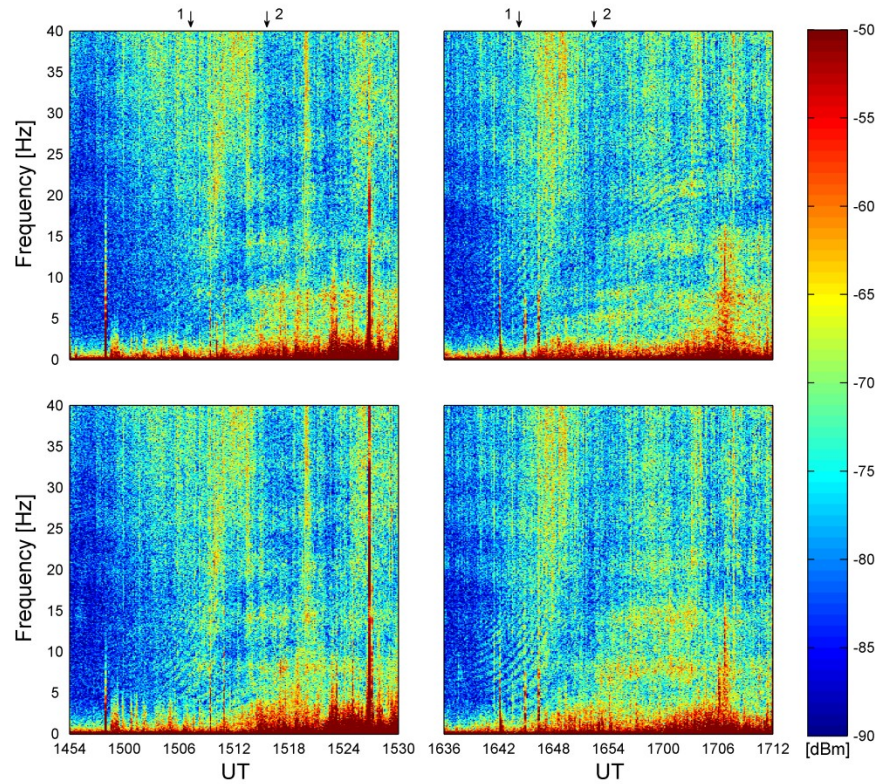
Figure 2: ELF spectrograms of the (top) meridional/vertical and (bottom) zonal/east-west electric field components measured with VEFI during orbits (left) 666 and (right) 667 on 31 May 2008. The resonator dispersion signature is the pattern resembling to a fingerprint visible in the bottom-left corner of each plot (1500-1512 and 1636-1648 UT). In the top-right panel, narrow lines are ubiquitous in the spectrogram (1639-1705 UT). The arrows indicate time of (1) sunset and (2) satellite eclipse. C/NOFS coordinates during IAR observation: altitude ⇒ 650-500 km, 600-450 km; latitude ⇒ 9°S-13°S, 11°S-13°S; longitude ⇒ 10°E-50°E, 20°W-20°E, for orbits 666 and 667, respectively.

582

583

584

585
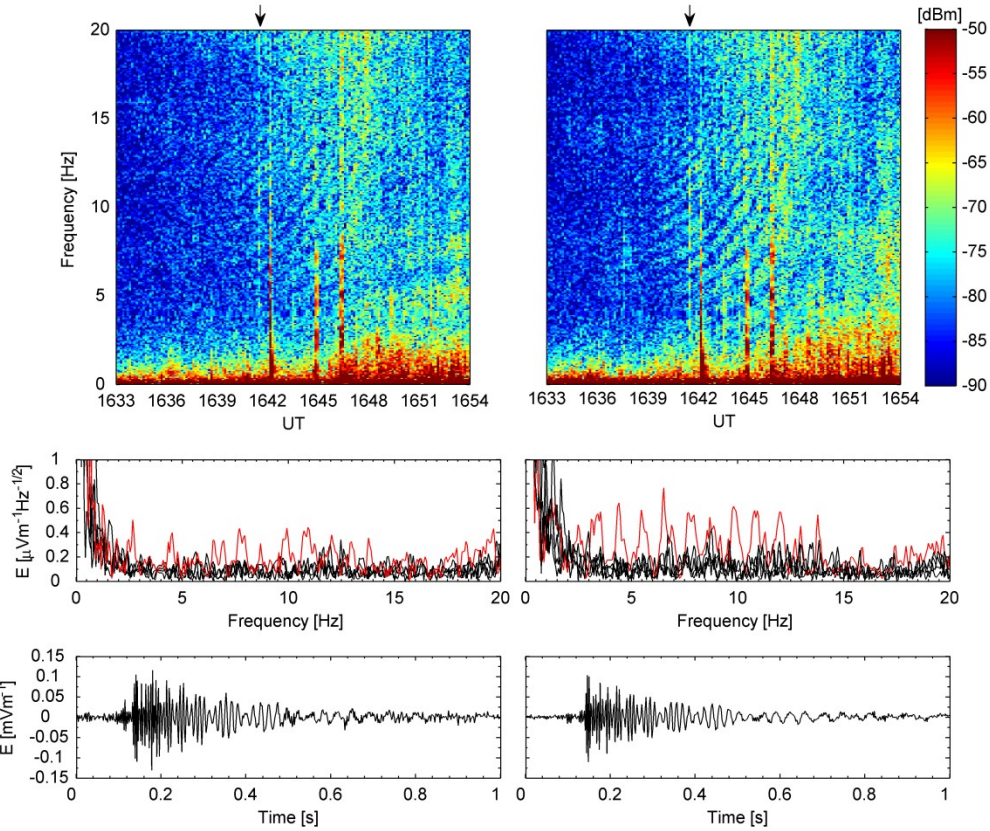
Figure 3: Spectra and waveforms of the (left) meridional and (right) zonal ELF electric fields measured during orbit 667. (Top) The arrows identify an interesting event starting at about 16:41:24 UT. The 3 strongest vertical lines in the spectrograms are satellite-related artifacts. (Middle) Spectral line of the event (red) and contiguous lines (black) for background noise comparison purposes. Note the peak amplitude sudden variation at about 14 Hz. (Bottom) Electric field waveforms of the event after removing the DC component.

592
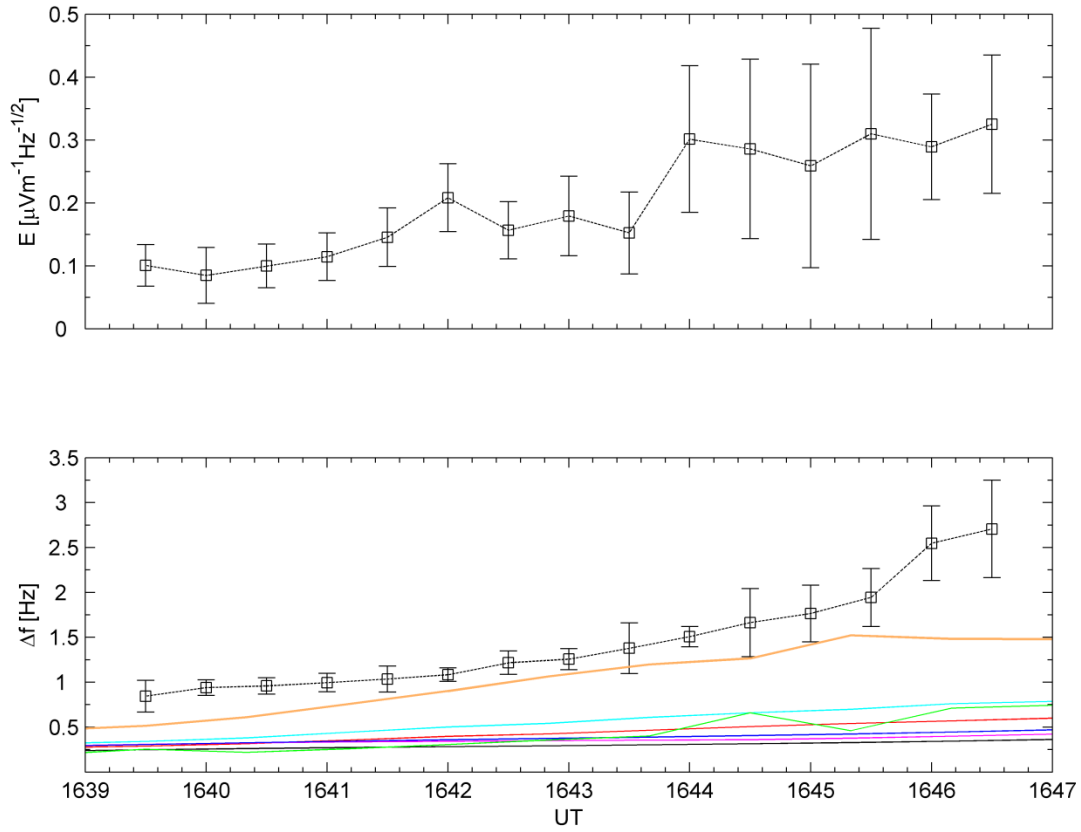
Figure 4: (Top) Electric field amplitude, *E*, and (bottom) frequency difference between consecutive peaks, Δ*f*, of the IAR modes evaluated from the zonal component about the terminator in the range 0-20 Hz. The mean and standard deviation of the zonal component are computed considering 30 s bins. The error bars indicate the standard deviation of each sample, where the sample size varies between 3 and 14, depending on the number of lines resolved in the spectrogram. The solid lines P0-P6 are computed with the MHD numerical model for composite plasma density profiles (see text for details); color code: P0 (black), P1 (red), P2 (cyan), P3 (magenta), P4 (blue), P5 (orange), and P6 (green).

601
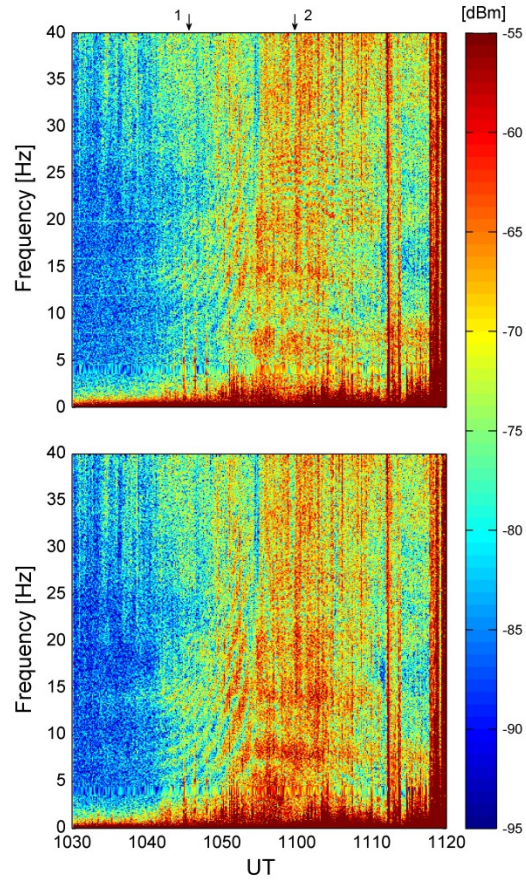
Figure 5: ELF spectrograms of the (top) meridional/vertical and (bottom) zonal/east-west electric field components measured with VEFI during orbit 694 in 2 June 2008. In addition to the IAR structure, the lowest Schumann resonance signatures, identified as fuzzy horizontal lines at about 8, 14, and 20 Hz, are also noticeable in the horizontal component. The arrows indicate time of (1) sunset (1049 UT) and (2) satellite eclipse (1058 UT). The IAR frequencies seem to increase drastically at 1054 UT. C/NOFS coordinates during IAR observation: altitude $\Rightarrow$ 750-550 km; latitude $\Rightarrow$ 10°S-13°S; longitude $\Rightarrow$ 40°E-100°E.
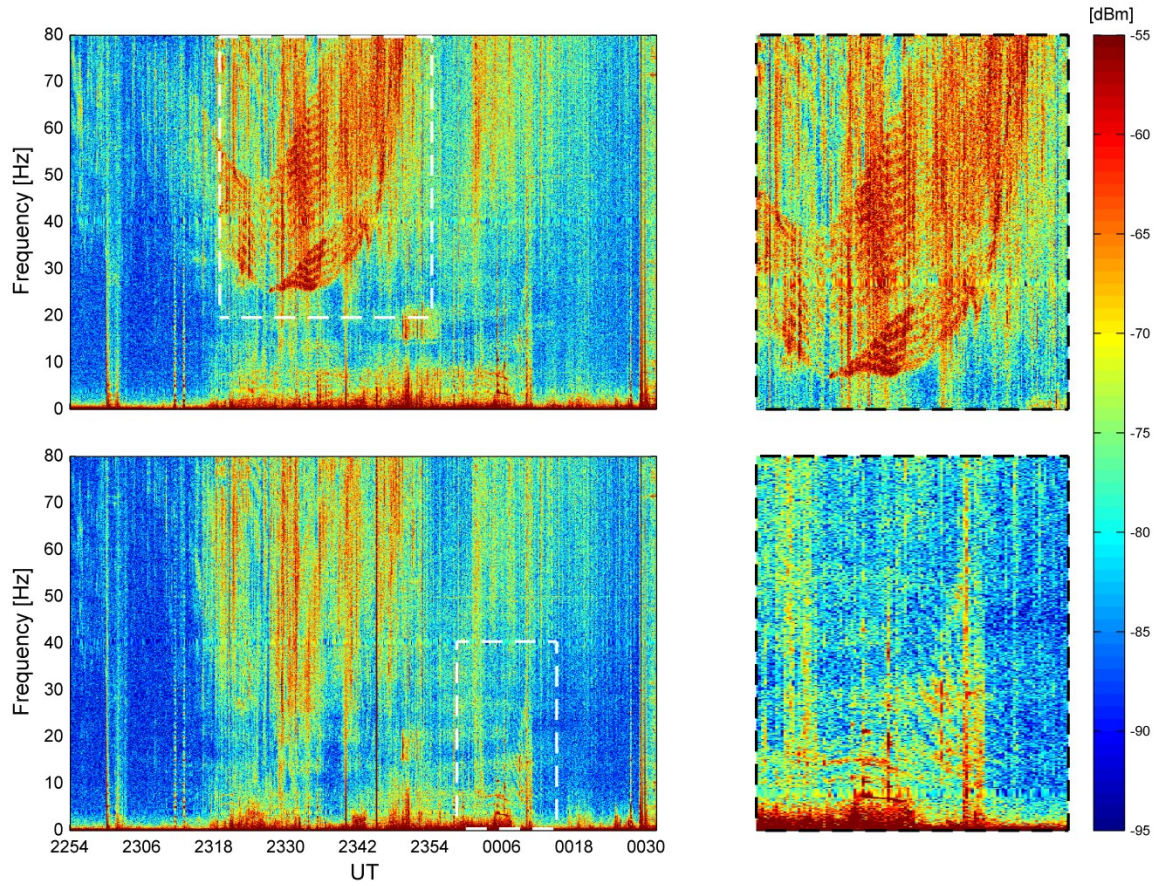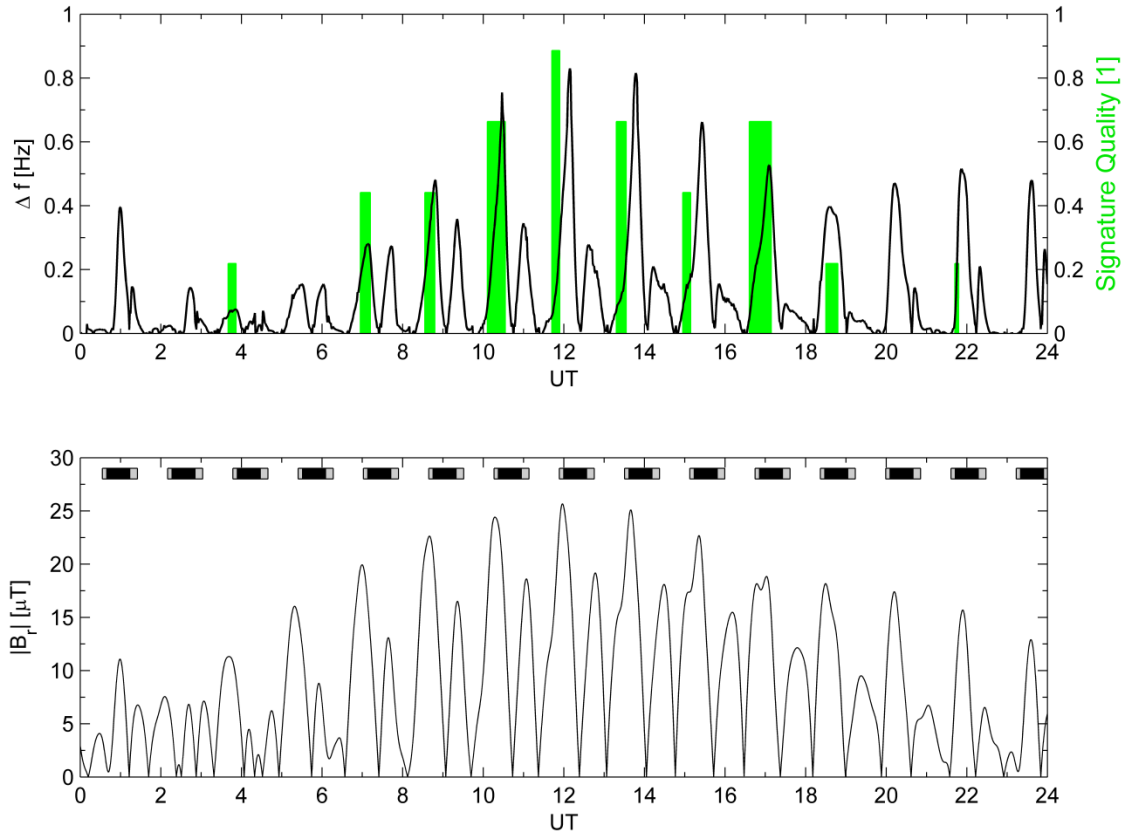
612

Figure 6: ELF spectrograms of the (top) meridional and (bottom) zonal electric field components

measured with VEFI during orbit 2898, in 28-29 October 2008. The white rectangles delimit the

detailed views shown in the right-hand-side. C/NOFS coordinates during IAR observation:

altitude $\Rightarrow$ 400-480 km; latitude $\Rightarrow$ 6°S-10°S; longitude $\Rightarrow$ 80°E-120°E.

617

618

619

620

621

622

Figure 7: Comparison between IAR model predictions using IRI-2007 default parameterization and VEFI measurements in 31 May 2008. (Top) The solid line indicates the Δf of the resonator computed with the IAR model. The green bars show when the fingerprint is identified in C/NOFS data; bar height subjectively assesses fingerprint quality (legibility, intensity, resolvability). The IAR signature is clearly observed in 10 out of 15 consecutive orbits. (Bottom) Average magnetic field radial component, B_r, in the altitude range 10^2-10^3 km at the satellite latitude/longitude; the gray and black markers represent nighttime on the ground and along satellite path, respectively.